iJRASET
International Journal For Research in Applied Science and Engineering Technology

INTERNATIONAL JOURNAL FOR RESEARCH

IN APPLIED SCIENCE & ENGINEERING TECHNOLOGY

Volume: 13 **Issue:** VII **Month of publication:** July 2025

DOI: https://doi.org/10.22214/ijraset.2025.73500

www.ijraset.com

Call: 08813907089 | E-mail ID: ijraset@gmail.com

International Journal for Research in Applied Science & Engineering Technology (IJRASET)
ISSN: 2321-9653; IC Value: 45.98; SJ Impact Factor: 7.538
Volume 13 Issue VII July 2025- Available at www.ijraset.com

Structural and Thermal Characterization of Geothermal Resources Using Aeromagnetic, Gravity, and Remote Sensing Data for Renewable Energy Exploration in North Eastern Chad Basin, Nigeria

Babagana A.Mustapha[1], Muhammad Muhammad Bello[2], Umar Suleiman[3], Sadiya Ahmad Muhammad[4], Mohammed Ibrahim Musa[5], Abba Kaka Alhaji Modu[6], Idris El-Yakub[7], Amina Jibril Muhammad[8]
[1, 2, 4, 6, 8]*Faculty of Physical Science Department of Physics Bayero University*
[7]*Faculty of Science, Department of Physics, University of Maiduguri*
[3]*National Centre for Remote Sensing Jos*

Abstract: ***This study integrates aeromagnetic, gravity, and remote sensing datasets to assess the geothermal potential of the northeastern Chad Basin, Nigeria. The Total and residual magnetic intensity maps reveal magnetic anomalies ranging from 32918 to 33184.5 nT, and -58.7 to147.8nT linked to shallow intrusions and hydrothermally altered zones. Vertical derivative and analytic signal processing delineate structurally complex zones favorable for geothermal activity, while Source Parameter Imaging (SPI) and Curie Point Depth (CPD) analysis estimate geothermal gradients and heat flow, identifying high-potential blocks such as Block 2 and Block 6 with heat flows exceeding 340 mW/m² and Curie depths ranging from 8.49 to 19.87 km. Gravity data further support these findings by highlighting low-density anomalies and structural breaks that may enhance geothermal fluid movement, with Bouguer anomaly values ranging between -47.2 and -37.1 mGal. Remote sensing analysis identifies dense lineament trends (NE–SW and NW–SE), hydrothermal alterations, and high land surface temperatures, with LST values between 289.85 and 339.7 K, correlating with underlying geophysical anomalies. The integration of these methods confirms spatial consistency in geothermal indicators across geologically and structurally favorable zones, notably around Mafa (13°22'E, 12°08'N), Kesangala (13°25'E, 12°15'N), Monguno (13°37'E, 12°40'N), and Konduga (13°25'E, 11°57'N). These results underscore the basin's elevated geothermal potential and provide a basis for targeted exploration and development***
Keywords: Curie point Depth,Geothermal gradients,land surface temperatures,hydrothermal alterations, Renewable Energy

I. INTRODUCTION

The increasing global demand for sustainable and renewable energy sources has positioned geothermal energy as a vital component of the low-carbon energy transition. Unlike solar or wind energy, geothermal resources offer base-load power generation with minimal environmental footprint, making them especially valuable in energy-deficient regions such as northeastern Nigeria (Lund & Toth, 2021; IEA, 2022). Effective exploration of geothermal resources requires integrated methods capable of identifying subsurface heat anomalies, structural controls, and geological conditions conducive to geothermal activity (Eppelbaum et al., 2014; DiPippo, 2016).

Recent advances in geophysical and remote sensing technologies have improved the efficiency of geothermal resource detection. Aeromagnetic data have proven effective in identifying buried faults, intrusive bodies, and fractures that serve as conduits for geothermal fluids (Reeves, 2005; Hinze et al., 2013). Techniques such as Reduction to the Equator (RTE), Reduction to the Pole (RTP), Analytic Signal (AS), First Vertical Derivative (FVD), Center for Passive Depth (CPD), and 2D/3D structural mapping (Zt, Zo, Zb) help delineate structural patterns, determine magnetic basement depths, and estimate geothermal gradients (Nwankwo et al., 2012; Ebong et al., 2022; Mogaji et al., 2017). These features are critical in understanding the geothermal heat transport mechanisms and targeting prospective zones.

©IJRASET: All Rights are Reserved

Gravity data complements aeromagnetic interpretation by highlighting density contrasts and subsurface mass distributions that may relate to heat sources such as magmatic intrusions or low-density sedimentary basins favorable for geothermal reservoirs (Telford et al., 1990; Fedi & Florio, 2001). The integration of gravity anomalies with magnetic and structural features enables a more comprehensive crustal characterization for geothermal assessment.

Remote sensing techniques provide additional surface and near-surface thermal indicators. Parameters such as Top-of-Atmosphere (TOA) reflectance, Brightness Temperature (BT), Normalized Difference Vegetation Index (NDVI), Proportion of Vegetation (Pv), land surface emissivity, and Land Surface Temperature (LST) are instrumental in detecting surface thermal anomalies, vegetation stress, and surface moisture conditions related to geothermal processes (Jiménez-Muñoz et al., 2009; Sobrino et al., 2004; Mallick et al., 2008). NDVI and Pv values help assess vegetation cover, which often reacts to geothermal emissions, while emissivity and LST provide thermal signatures indicating anomalous subsurface heat flow (Weng, 2009; Guha et al., 2013).

In arid to semi-arid regions like the northeastern Chad Basin of Nigeria, characterized by high geothermal gradients, crustal thinning, and active tectonics, this multi-technique approach holds substantial promise (Mogaji et al., 2017; Ajakaiye et al., 1981). However, despite these favorable conditions, the region remains underexplored. Previous studies in other regions have demonstrated the success of combining magnetic, gravity, and thermal remote sensing data in identifying and characterizing geothermal fields (Noorollahi et al., 2008; Baioumy & Tada, 2022; Sadeghi et al., 2023).

This study aims to structurally and thermally characterize geothermal resources in the northeastern Chad Basin using a fusion of aeromagnetic, gravity, and remote sensing datasets. The approach techniques such as, Analytic signal, First Vertical Derivative, Curie Point Depth, and temperature gradient analysis from aeromagnetic data; Bouguer and residual anomaly modelling from gravity data; and Top of Atmospheric, Brightness Temperature, Normalised DifferenceVegetation Index, Proportion vegetation, Emissivity Surface Temperature andLand Surface Temperature, and analysis from Landsat imagery. The result will contribute toward identifying geothermal targets for future energy development in Nigeria and support the country's climate and energy transition strategies.

A. Location and geologic settings of the study area

The geological map illustrates that the entire study region falls within the Quaternary formation**,** highlighted in yellow. This formation is known to consist of unconsolidated sediments such as sand, silt, clay, and gravel, typically deposited during the most recent geological period the Quaternary, which spans the last 2.6 million years to the present.

The map extends geographically from approximately 12°00′ to 12°30′N latitudeand13°00′ to 13°30′E longitude**,** covering areas like Konduga, Jere, Monguno, Mafa, Kilborani, Gajiram**,** and Ajiri**.** These towns are all located within this widespread Quaternary zone.

This geological setting suggests that the region is relatively young in geologic time, possibly formed by fluvial, lacustrine, or Aeolian processes, which are common in sedimentary environments. The presence of extensive Quaternary deposits often correlates withflat topography**,** good groundwater potential, and agricultural suitability, but may also indicate higher susceptibility to erosion or seasonal flooding due to loose sediment composition.

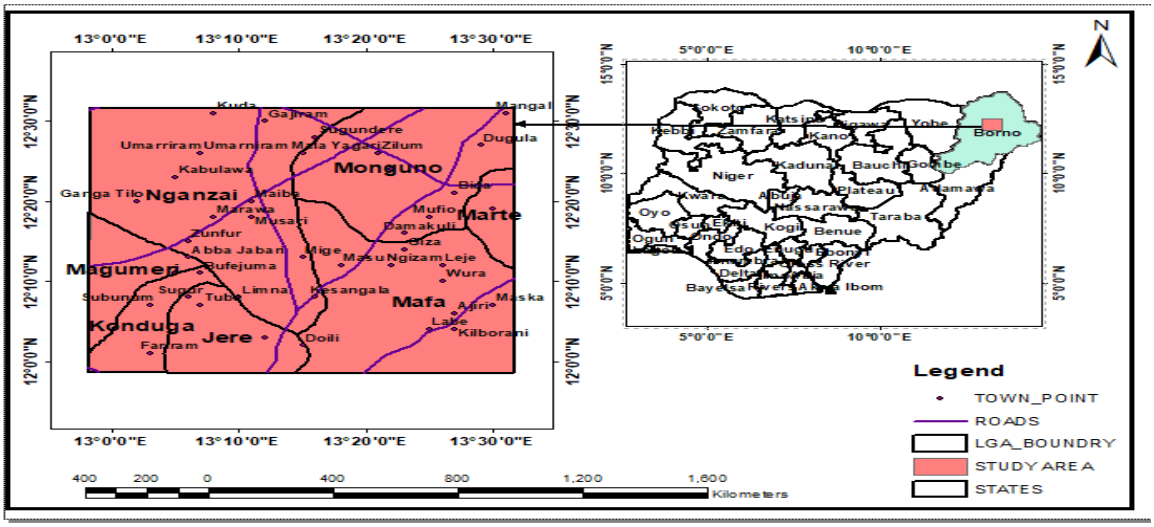

Figure 1: Location Map of the study area, source (Modified by the Author using QGIS)

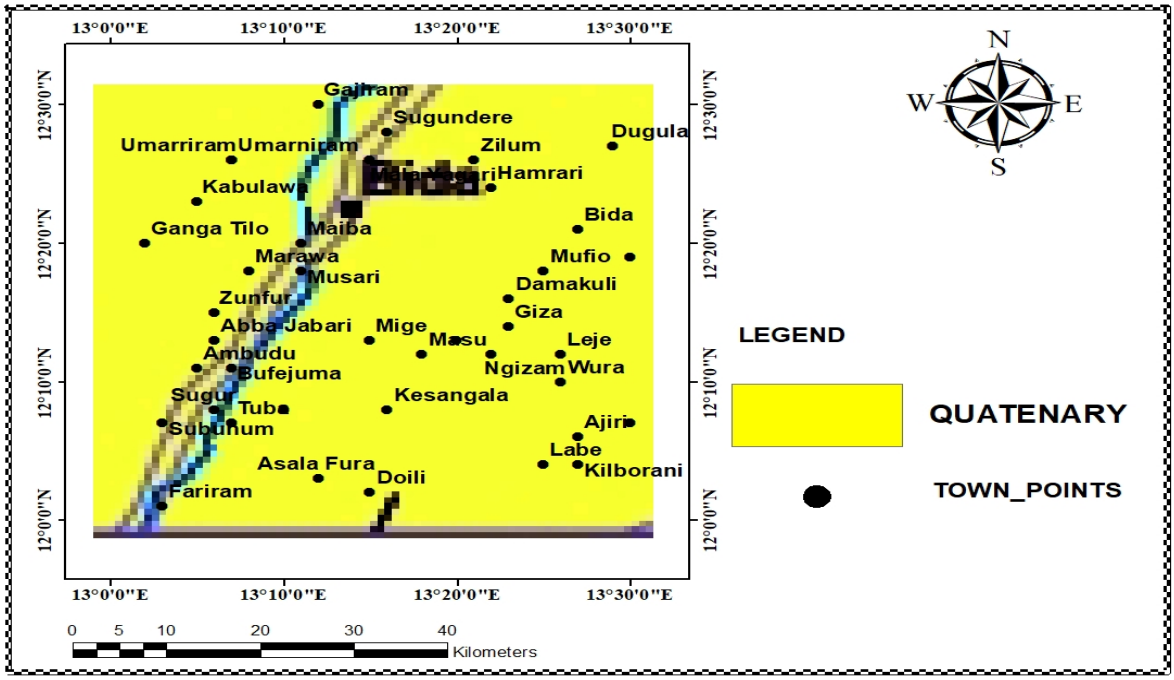

Figure 2: Geologic Map of the Sheet 67 Chad basin, modified after Nigerian Geological Survey Agency (NGSA 2007)

II. THEORY OF METHODS ANALYSIS

A. *Magnetic Method*

Geological Structural Setting

1) *First Vertical Derivative (FVD)*

The First Vertical Derivative (FVD) map enhances shallow magnetic anomalies linked to near-surface geological features. It emphasizes high-frequency signals while reducing deeper source effects. As noted by Remke et al. (2004), FVD is computed by differentiating the total magnetic field vertically.

$$FVD = \frac{\partial M}{\partial z} (1)$$

2) *Analytical Signal (AS) Technique*

The Analytical Signal (AS) technique is effective for interpreting magnetic and gravity data as it is independent of magnetization direction and contrast. For 2D bodies, it produces a symmetric, bell-shaped response, while in 3D, it is enhanced using the three orthogonal gradients of the total magnetic field. As described by Remke et al. (2004), the 3D AS at a location (x, y) is calculated from the vector magnitude of these gradients, making it useful for identifying source edges.

$$|A(x,y,z)| = \sqrt{\left(\frac{dT}{dx}\right)^2 + \left(\frac{dT}{dy}\right)^2 + \left(\frac{dT}{dz}\right)^2} \quad (2)$$

Where |A(x, y, z)| is the amplitude of the analytical signal at (x, y, z) and T is the observed magnetic field at (x, y, z).
Thermal structural mapping and heat flow Spectral depth analysis theory

B. *The Centroid Method*

Curie point depth estimation using the centroid method involves calculating the top and centroid depths of magnetic sources from the power spectrum of magnetic data (Bansal et al., 2016). This spectrum relates to the depth and thickness of the magnetic body (Blakely, 1996). The magnetic anomaly represents variations caused by subsurface structures with differing magnetic properties.

$$P(K_x K_y) = 4\pi^2 C_m^2 \varphi_m(K_x K_y) |\theta_m|^2 |\theta_f|^2 e^{-2|k|z_t} \times \left(1 - e^{-|k|(z_b - z_t)}\right)^2 (3)$$

K_x and K_y are the respective wave numbers, Cm is the constant of proportionality, ϕ is the power spectrum of magnetization and geomagnetic field, Z_t and Z_b are the top to bottom depth respectively. θ_m and θ_f becomes constant by taking the radial average, as equation 2 becomes

$$P(K) = A_1 e^{-2|k|z_t} \times \left(1 - e^{-|k|(z_b - z_t)}\right)^2 \quad (4)$$

For a very thick magnetic body, the right hand side of equation 3 remains constant, and A_1 also remain constant as such the above equation reduces to

$$P(K) = A_1 e^{-2|k|z_t} \quad (5)$$

Equation 4 above can be used in evaluating top depth of an anomalous magnetic body, and the centroid depth of magnetic body can express as

$$\ln\left(\frac{P(K)^{\frac{1}{2}}}{K}\right) = A_2 - |k|Z_0 \quad (6)$$

The Curie point depth is finally, the depth calculated using the top and centroid depths. And is express as follows

$$Z_b = 2Z_0 - Z_t \quad (7)$$

The centroid method is widely used to estimate Curie point depth from aeromagnetic data, providing insight into geothermal potential. Temperature typically increases by 25°C per kilometre with depth, representing the geothermal gradient (State, 2021). This gradient is linked to heat flow through Fourier's law in a one-dimensional Earth model (Quintero et al., 2019).

$$q = \lambda(dT/dz) \quad (8)$$

Where:

q Is the heat flow

λ Is the thermal conductivityof 2.5 W/m/°C as the average for igneous rocks and a Curie temperature of 580°C are used as standard(Quintero et al., 2019)

(dT /dZ) is the geothermal gradient

The Curie temperature V can also be defined as;

$$V = (dT/dz)Z_B \quad (9)$$

Where:

Z_B Is the Curie point depth or basal depth.

The relationship between heat flow, Curie temperature, and Curie point depth is given as

$$q = \lambda\left(V/Z_B\right) \quad (10)$$

C. Remote Sensing Method

Thermal Surface structural mapping

Step 1: Obtain Satellite Data

Use TIR bands from satellite sensors such as:

Landsat 8/9: Band 10 (10.6–11.19 µm)

Step 2: Convert Digital Number (DN) to Top of Atmosphere (TOA) Spectral Radiance

Equation:

$L\lambda = ML \times Qcal + AL \quad (11)$

Where:

Lλ: TOA spectral radiance (W/m²·sr·µm)

ML: Radiance multiplicative scaling factor (from metadata)

AL: Radiance additive scaling factor (from metadata)

Qcal: Quantized calibrated pixel value (DN)

Step 3: Convert TOA Radiance to Brightness Temperature (BT)

The metadata attached to Landsat 8 scene contains the constant thermal values. These values are used to convert spectral radiance to the BT from Kelvin (K)

$$TB = \frac{K_2}{Ln(K_1/L\lambda + 1)} \quad (12)$$

Where:

TB: Brightness Temperature in Kelvin

K1, K2: Thermal conversion constants (from metadata)

Lλ: TOA spectral radiance

Step 4: Calculate NDVI for Emissivity Correction

Calculate Normalized Difference Vegetation Index NDVI is a standard vegetation index used to estimate the vegetation health and can be calculated using the Near-infrared (band 5) and Red (band 4) bands. It is expressed thus

$$NDVI = \frac{(\text{NIR} - \text{RED})}{(\text{NIR} + \text{RED})} \quad (13)$$

$$NDVI = \frac{(Band5 - Band4)}{(Band5 + Band4)} \quad (14)$$

For Landsat 8/9:

Where;

Red = Band 4

NIR = Band 5

Step 5: Estimate Proportion of Vegetation (PV)

Equation: Calculate Land Surface Emissivity E accounts for the mean emissivity of a component on the earth surface. It is calculated from the NDVI. Before calculating the E, the Proportion of Vegetation (PV) is premeditated first, as shown in equation

$$Pv = \left(\frac{\text{NDVI} - \text{NDVImin}}{\text{NDVImax} - \text{NDVImin}}\right)^2 \quad (15)$$

Where:

NDVImin, NDVImax: Minimum and maximum NDVI

Step 6: Calculate Surface Emissivity (ε)

Equation:

$\varepsilon = 0.004 \times Pv + 0.986$ (16)

Or use land cover-specific values as needed.

Step 7: Calculate Land Surface Temperature (LST)

Finally, to calculate the LST, the below equation is used

$$LST = \frac{TB}{[1 + (\lambda \times \text{TB} / \rho) \times \ln(\varepsilon)]} \quad (17)$$

Where:

LST: Land Surface Temperature in Kelvin

TB: Brightness temperature (K)

λ: Wavelength of emitted radiance (~10.895 μm for Landsat 9 Band 10)

ε: Surface emissivity

$\rho = h \cdot c / \sigma = 1.438 \times 10^{-2}$ m·K

Constants:

h: Planck's constant (6.626×10^{-34} J·s)

c: Speed of light (2.998×10^{8} m/s)

σ: Boltzmann constant (1.38×10^{-23} J/K)

III. METHODOLOGY

This study integrates remotely sensed and geophysical datasets within a Geographic Information System (GIS) framework to assess the potential for geothermal manifestations using both qualitative and quantitative techniques. All spatial data were standardized by georeferencing and projecting them to a consistent geographic coordinate system to facilitate integrated spatial analysis.

Land Surface Temperature (LST) was extracted from Landsat 9 imagery to identify surface thermal anomalies that may indicate geothermal activity. Each Landsat 9 scene includes 11 spectral bands (Bands 1–11), many of which are ambiguously named. For the purpose of Land Surface Temperature (LST) analysis, Bands 10, 5, and 4were selected representing thermal infrared, near-infrared, and red bands, respectively. These bands were utilized within the ArcMap environment using the Raster Calculator to derive LST Subsurface geological features associated with geothermal systems were delineated through the interpretation of gravity and magnetic anomaly data, as represented in the conceptual model.

Lineament and lineament density maps, which provide critical information on structural controls of geothermal systems, were derived from Advanced Space borne Thermal Emission and Reflection Radiometer Digital Elevation Model (ASTER DEM) data. These structural features were used to infer potential conduits for heat and fluid flow from the subsurface to the surface.

A. Data Collection

Landsat 9 satellite imagery covering the study area was downloaded from the United States Geological Survey (USGS) Earth Explorer portal (http://earthexplorer.usgs.gov) on July 16, 2025. Scenes were selected to fully encompass the target area, specifically corresponding to path/row 185/52.and also ASTER Global Digital Elevation Model (ASTER GDEM) was utilized to obtain elevation data for the study area. Developed jointly by NASA and Japan's METI, the ASTER GDEM provides global elevation coverage at a spatial resolution of 30 meters. It is widely used for topographic analysis, geomorphological mapping, and geophysical modelling. In this study, ASTER DEM data supports terrain correction, structural interpretation, and integration with other geophysical datasets. The dataset was downloaded freely from the NASA Earth data portal (https://earthdata.nasa.gov)TheBureau Gravimétrique International (BGI) provides a global archive of terrestrial, marine, airborne, and satellite gravity data, widely used in geophysical and geological research. Accessible at http://bgi.obs-mip.fr, it operates under the IAG and is part of the IGFS**.** BGI includes data from satellite missions such as GRACE (2002) and GOCE (2009), with resolutions ranging from 70–110 km, while regional grids can reach up to 5 km or finer. Its datasets cover Bouguer and free-air anomalies, gravity disturbances, and geoid heights. In this study, BGI gravity data supports detailed subsurface modelling and enhances geological interpretation when integrated with aeromagnetic data (Sandwell et al., 2013). In addition, high-resolution aeromagnetic data were obtained from the Nigerian Geological Survey Agency (NGSA). These data were acquired and processed by Fugro Airborne Surveys as part of a national survey campaign conducted between December 2006 and May 31, 2007.

IV. RESULTS AND DISCUSSION

The Total Magnetic Intensity (TMI)Figure (3a)ranges from 32,918 to 33,184.5 nT, highlighting magnetic susceptibility variations linked to geological structures. High TMI values (pink to red) are concentrated in the northeastern and central parts of the area approximately between 12°15′ to 12°30′ Nand 130°15′ to 130°30′ Esuggesting shallow magnetic bodies like mafic or intermediate intrusions that may act as heat sources. Lower values (blue to green), found in the southwestern and western zones (12°00′ to 12°15′ N, 130°00′ to 130°15′ E), are likely associated with hydrothermally altered rocks, possibly marking geothermal fluid pathways.

The Residual Magnetic Intensity (RMI)Figure (3b) ranges from −58.7 to +147.8 nT, revealing localized shallow magnetic contrasts. High residual anomalies are concentrated in the north-central and northwestern areas(12°15′–12°25′ N, 130°00′–130°20′ E), pointing to shallow intrusions or magnetite-rich zones. Low RMI values are observed in the southwestern and southeasternregion**s** (12°00′–12°15′ N, 130°00′–130°30′ E), potentially reflecting demagnetized rocks due to hydrothermal processes.

A. Delineation of Structural Trend

The First Vertical Derivative (FVD**)**Figure (3c) highlights magnetic gradients, delineating near-surface structural features. High FVD values (pink to red) appear in the central, western, andsoutheastern portions (12°00′–12°25′ N, 130°00′–130°30′ E), indicating zones of structural complexity with faults and fractures. Lower FVD values (blue to green) dominate the **north-**central and northeastern parts (12°20′–12°30′ N, 130°10′–130°30′ E), reflecting deeper or more uniform magnetic sources.

Figure (3d)Analytic Signal (AS) values reach up to 0.067 nT/m, emphasizing subsurface magnetic edges. High AS values are located in the southwestern, southeastern, and northwestern zones (12°00′–12°25′ N, 130°00′–130°30′ E), representing structurally complex, shallow sources favorable for geothermal fluid movement. Lower AS values are observed in the central zone (12°10′–12°25′ N, 130°15′–130°25′ E), indicating more homogeneous or deeper geology.

The lineament Figure (3e)supports this structure, showing dominant orientations of northeast–southwest and northwest–southeast, aligning with magnetic trends. Densely fractured zones lie near towns like Kesangala, Giza, Dutsin Dogo, and Magumeri, marking structurally favorable geothermal targets.

The Source Parameter Imaging (SPI**)** Figure (3f) estimates depths to magnetic sources from 180 m to over 900 m. Deeper sources (blue shades) are mainly in the central and northeastern areas (12°15′–12°25′ N, 130°15′–130°30′ E), indicating buried intrusions or deep-seated faults as potential heat sources. Shallower depths (pink to red) dominate the southern and western zones (12°00′–12°15′ N, 130°00′–130°20′ E), favorable for reservoir development and fluid flow.

©IJRASET: All Rights are Reserved | SJ Impact Factor 7.538 | ISRA Journal Impact Factor 7.894 |

International Journal for Research in Applied Science & Engineering Technology (IJRASET)
ISSN: 2321-9653; IC Value: 45.98; SJ Impact Factor: 7.538
Volume 13 Issue VII July 2025- Available at www.ijraset.com

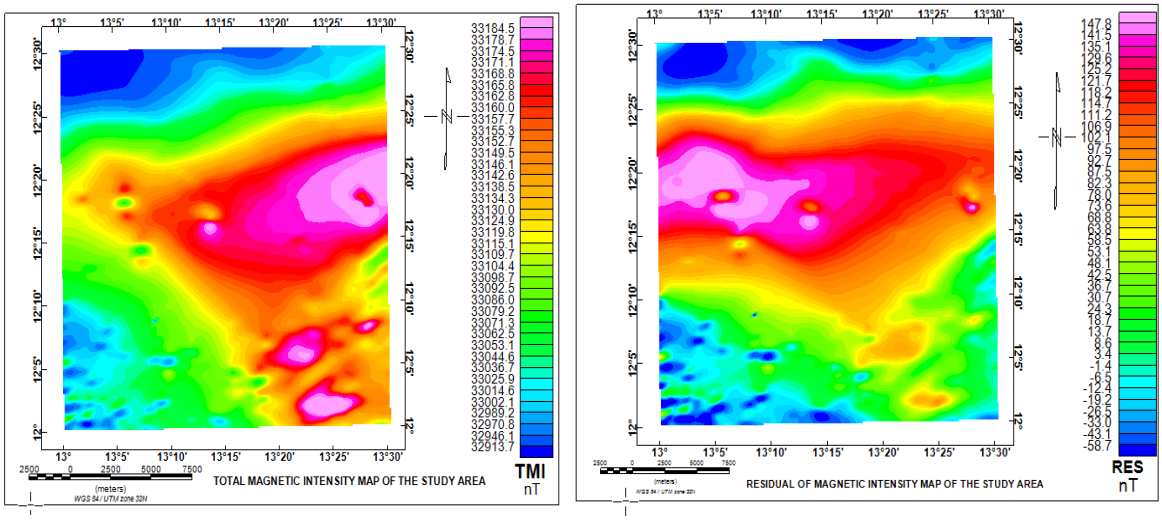

Figure 3: (a) Total magnetic intensity map and (b) RMI residual Magnetic Intensity map of the study area

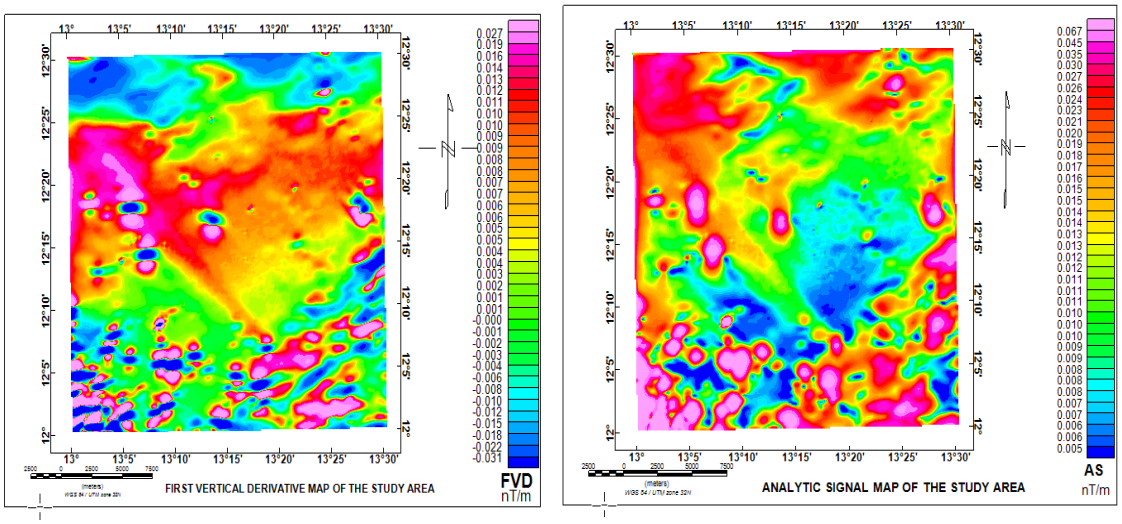

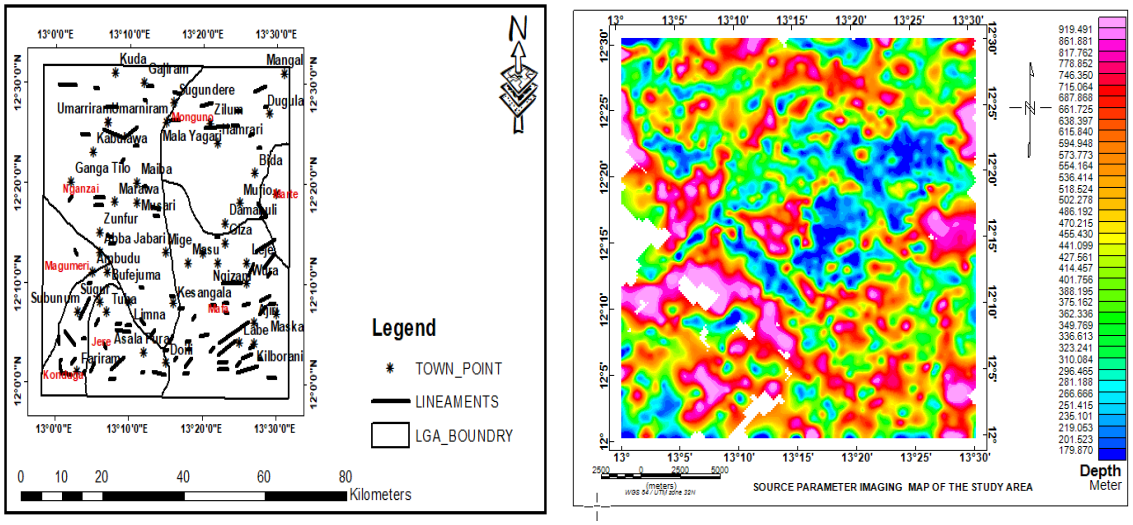

Figure 3: (c) First Vertical derivative map (d) Analytical signal map (e) Lineament map and (f) Source Parameter Imaging map the of study area

©IJRASET: All Rights are Reserved | SJ Impact Factor 7.538 | ISRA Journal Impact Factor 7.894 |

ISSN: 2321-9653; IC Value: 45.98; SJ Impact Factor: 7.538
Volume 13 Issue VII July 2025- Available at www.ijraset.com

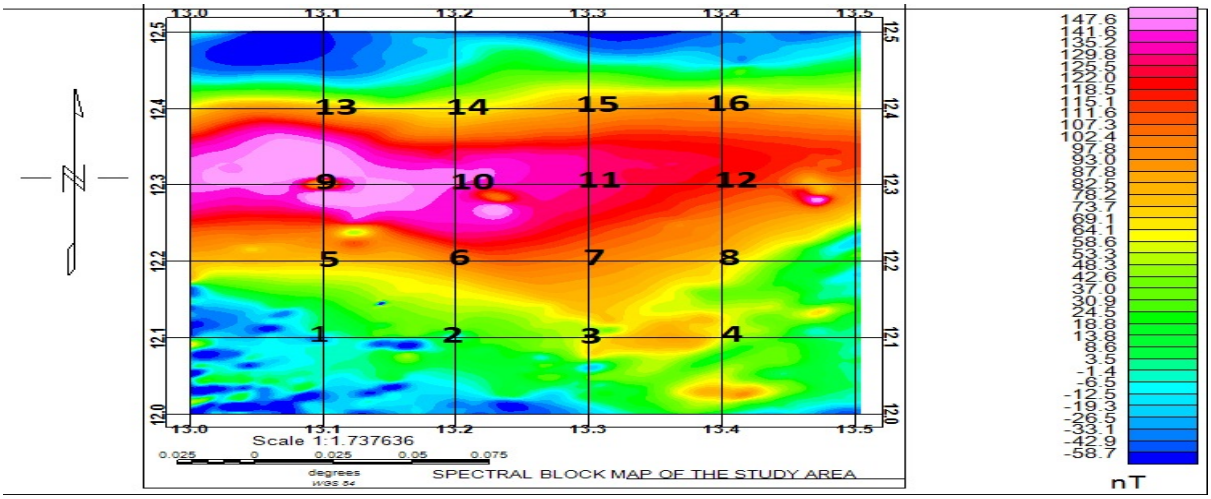

Figure 3 (g) Spectral Block Map of the Study Area

B. Estimating the Curie point depth, geothermal gradient, and heat flow

For this study, sixteen (16) overlapping sub-sheets were mapped out and each subjected to Fast Fourier Transform (FFT) analysis. This process decomposes the magnetic data into its wave and energy spectral components. Both components were plotted using EXCEL with the log of energy on the vertical axis and the wave-number component on the horizontal axis (Fig. 3h). A straight line is fitted at the lower and higher wave-number portions of the graph to generate gradients corresponding to the depth to the centroid (Zo) and depth to the top (Zt) of magnetic sources, respectively. The CPD is calculated from the values of depth to the centroid and top of magnetic sources using equation (7). The geothermal gradient was obtained when the Curie point depth is inputted into equation (8). Both CPD and geothermal gradient were used as inputs in equation (9) to evaluate the heat flow using a thermal coefficient of 2.5. The geothermal parameters were obtained for each of the sixteen blocks, and a coordinate corresponding to the centre of each block was recorded (Table 1). Recorded coordinates for sixteen blocks and values for each parameter were inputted into contouring software (Surfer Version 20). The resultant contour maps for Curie point depth, geothermal gradient, and heat flow were generated to show the prevailing trend of each parameter across the study area.

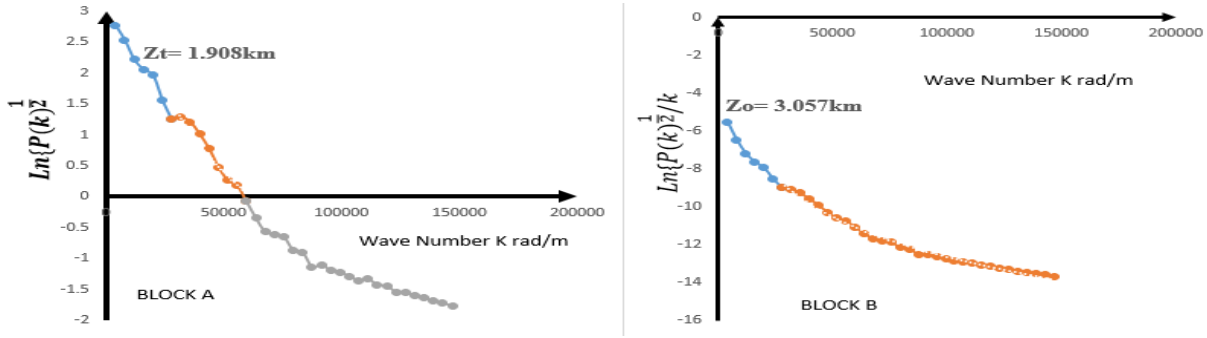

Figure: 3h Spectral plot for block A&B indicating depth to top (Zt) and centroid (Zo)

The spectral analysis across 16 blocks reveals Curie Point Depth (CPD) values ranging from 3.94 to 8.48 km, with an average of 6.28 km, indicating relatively shallow magnetic source depths and suggesting a thermally active crust. The geothermal gradient varies between 68.37 and 147.36 °C/km, averaging 96.42 °C/km, while heat flow values range from 170.93 to368.39 mW/m², with an average of 241.04 mW/m². The shallowest CPD and highest thermal signatures are observed in Blocks 2 and 6 (centered around 13.2°E, 12.2°N), confirming these as the most promising geothermal zones. These results reflect a high heat flux environment and support the presence of structurally controlled geothermal systems within the central and southwestern parts of the study area.

©IJRASET: All Rights are Reserved | SJ Impact Factor 7.538 | ISRA Journal Impact Factor 7.894 |

Table 1: Evaluated CPD, geothermal gradient, and heat flow of study area

SPECTRAL BLOCK	Zt depth(km)	Zo depth(km)	Currie depth (km)	Geothermal gradient (°C/ km)	Heat flow (mW/ m^2)	LONG	LAT
1	1.92	3.657	5.394	107.5268817	268.8172043	13.1	12.1
2	1.908	3.057	4.206	137.8982406	344.7456015	13.2	12.2
3	1.425	4.29	7.155	81.06219427	202.6554857	13.3	12.3
4	1.974	4.293	6.612	87.71929825	219.2982456	13.4	12.4
5	1.122	2.939	4.756	121.9512195	304.8780488	13.1	12.1
6	1.244	2.59	3.936	147.3577236	368.3943089	13.2	12.2
7	2.08	4.228	6.376	90.96612296	227.4153074	13.3	12.3
8	0.993	4.738	8.483	68.37203819	170.9300955	13.4	12.4
9	1.888	4.687	7.486	77.47795886	193.6948971	13.1	12.1
10	2.244	4.17	6.096	95.14435696	237.8608924	13.2	12.2
11	2.777	4.726	6.675	86.89138577	217.2284644	13.3	12.3
12	1.626	4.271	6.916	83.86350492	209.6587623	13.4	12.4
13	2.921	4.342	5.763	100.6420267	251.6050668	13.1	12.1
14	1.578	4.438	7.298	79.47382845	198.6845711	13.2	12.2
15	2.012	4.034	6.056	95.77278732	239.4319683	13.3	12.3
16	1.916	4.558	7.2	80.55555556	201.3888889	13.4	12.4
AVERAGE			6.2755	96.41719523	241.0429881		

C. Curie Depth Point (CDP) Map

The Curie Depth Point (CDP) model Figure (5a) delineates the base of the magnetically active crust, with depths varying from approximately 3.8 km to 8.8 km. The shallowest Curie depths (3.8–5.8 km) are dominantly situated in the south-western and central domains, indicative of elevated geothermal gradients and enhanced subsurface heat flow. Conversely, the northeastern and eastern sections are characterized by deeper Curie depths (>6.8 km), reflecting relatively cooler crustal conditions. These spatial patterns suggest thermally anomalous regions in the southwest, which are potentially conducive to geothermal exploration and development.

D. Geothermal Gradient Map

Geothermal gradient analysis Figure (5b) exhibits pronounced thermal heterogeneity across the study area, with values ranging from approximately 65°C/km in the northeastern and eastern zones to over 150°C/km in the south-western region. The maximum geothermal gradient is observed near 12.15°–12.20°N and 13.15°–13.20°E, corresponding to zones of minimal Curie depth, thereby affirming a region of significant crustal heat concentration. The observed gradient attenuates progressively toward the north and east, mirroring the transition into deeper Curie isotherms and suggesting a decline in geothermal potential in those areas.

E. Heat Flow Map

Figure (5c)heat flow distribution, bounded between latitudes 12.1°N–12.4°N and longitudes 13.1°E–13.4°E, demonstrates considerable spatial variability. The south-western quadrant records the highest heat flow intensities, exceeding 320 mW/m², particularly within 12.15°N–12.25°N and 13.15°E–13.25°E. This zone coincides with both elevated geothermal gradients and shallower Curie depths, signalling a potential geothermal anomaly of economic significance. Moderate heat flow values (270–310 mW/m²) dominate the central corridor, while the northeastern and southeastern extremities exhibit subdued values (170–220 mW/m²), reflecting diminished thermal activity and deeper lithospheric thermal boundaries.

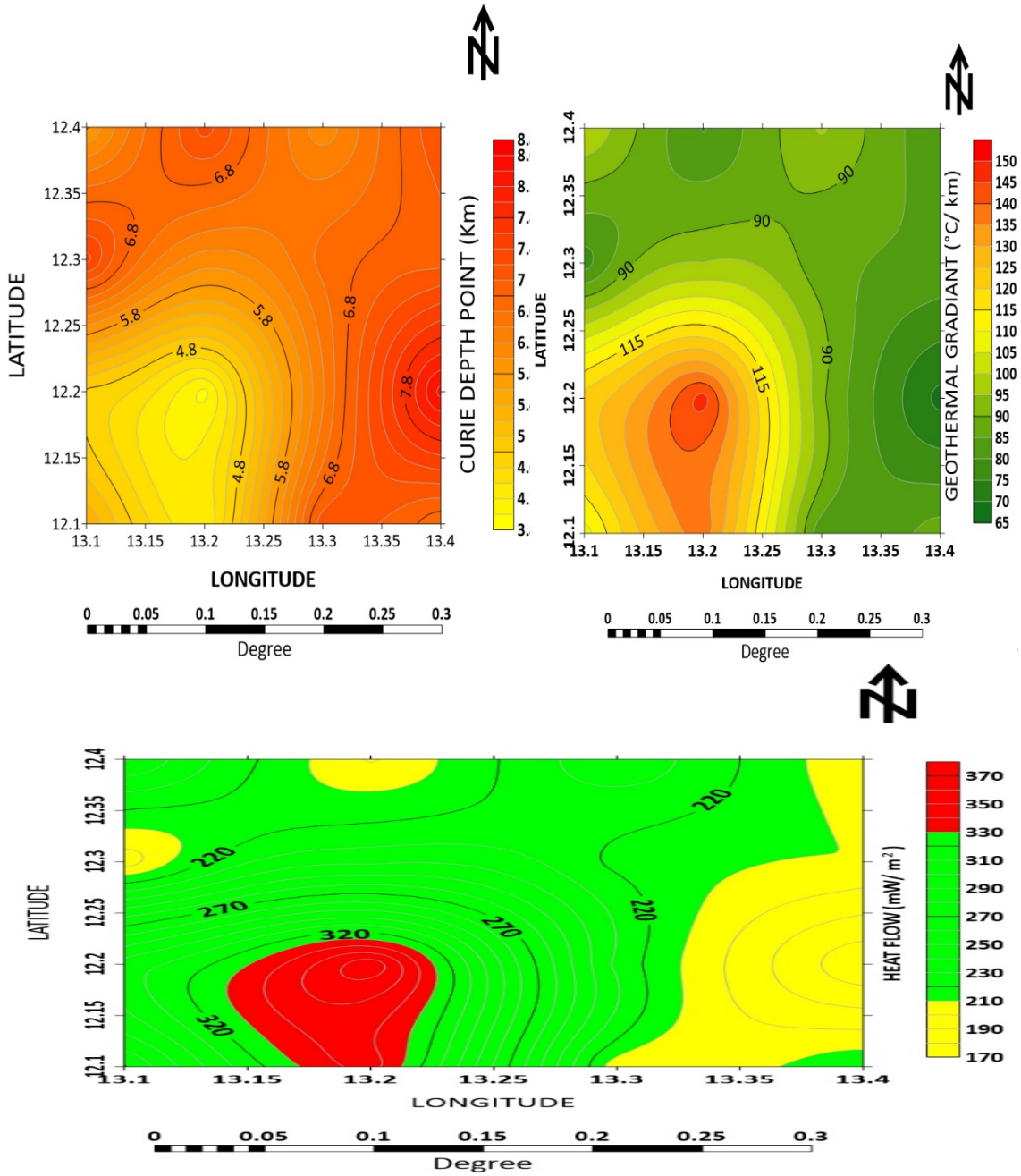

Figure 5: (a) Contour map of Curie Point Depth CPD (b) geothermal gradient and (c) heat flow of the study area

V. GRAVITY METHOD

The Bouguer Anomaly Figure (6a)shows gravity values ranging from 64.4 to 89.2 mGal, indicating subsurface density variations relevant to geothermal exploration. Low anomaly zones in the southwestern region (64–70 mGal) suggest low-density, possibly fractured or altered rocks that may serve as geothermal reservoirs due to higher porosity and permeability. High anomaly values in the eastern and northeastern parts (75–89 mGal) likely reflect denser basement rocks or intrusions, which could act as heat sources. The central transition zone marks potential faults or structural features that may enhance fluid circulation and heat transport, indicating favorable geothermal conditions.

The Residual Anomaly Figure (6b)reveals localized gravity variations, essential for identifying geothermal prospects. The southwestern zone (centered around 13°05′E, 12°05′N) shows the lowest residual anomalies (–12.15 mGal), indicating shallow low-density bodies like fractured or thermally altered rocks, ideal for geothermal fluid storage.

The northeastern and southeastern flanks exhibit higher residuals (~6.28 mGal), possibly due to denser, heat-conducting basement rocks. The gradient zones between low and high values suggest faults or fractures enhancing geothermal fluid movement, marking them as promising geothermal targets.

The First Vertical Derivative (FVD) Figure (6c) enhances shallow structures, crucial for geothermal targeting. The map reveals sharp gradient zones trending NE-SW and NW-SE, especially around 13°00′E to 13°15′E and 12°00′N to 12°20′N, suggesting fractures or faults that can act as pathways for geothermal fluids. These structural discontinuities are vital for heat transport and fluid circulation, making them priority zones for geothermal exploration.

The analytic signal (AS) Figure (6d)reveals significant spatial variations in subsurface structures across the study area, with amplitude values ranging from below 0.001 to above 0.01 mGal/m. High AS amplitudes, indicated by red to pink colors, are predominantly observed in the southern and southwestern portions of the map, approximately between coordinates 12°00'–12°15' N and 130°00'–130°30' E. These regions exhibit strong geophysical contrasts, likely associated with intrusive bodies, fault zones, or hydrothermally altered rocks, which are favorable conditions for geothermal activity.

Conversely, low AS values (blue to green colors) dominate the central and northeastern sectors of the map, extending roughly from 12°15' to 12°30' N and 130°15' to 130°30' E. These areas are interpreted to be geologically more homogeneous or deeper seated, with limited structural disruptions, suggesting lower geothermal potential.

A general northeast-southwest trending pattern is observed in the high-amplitude anomalies, implying a structural alignment that may reflect regional tectonic control. This structural trend is critical, as it may guide geothermal fluid migration and heat transport. In summary, the AS map delineates key geothermal targets in the southwest and southeast, with a notable northeast-southwest structural trend, warranting further geophysical and geochemical validation.

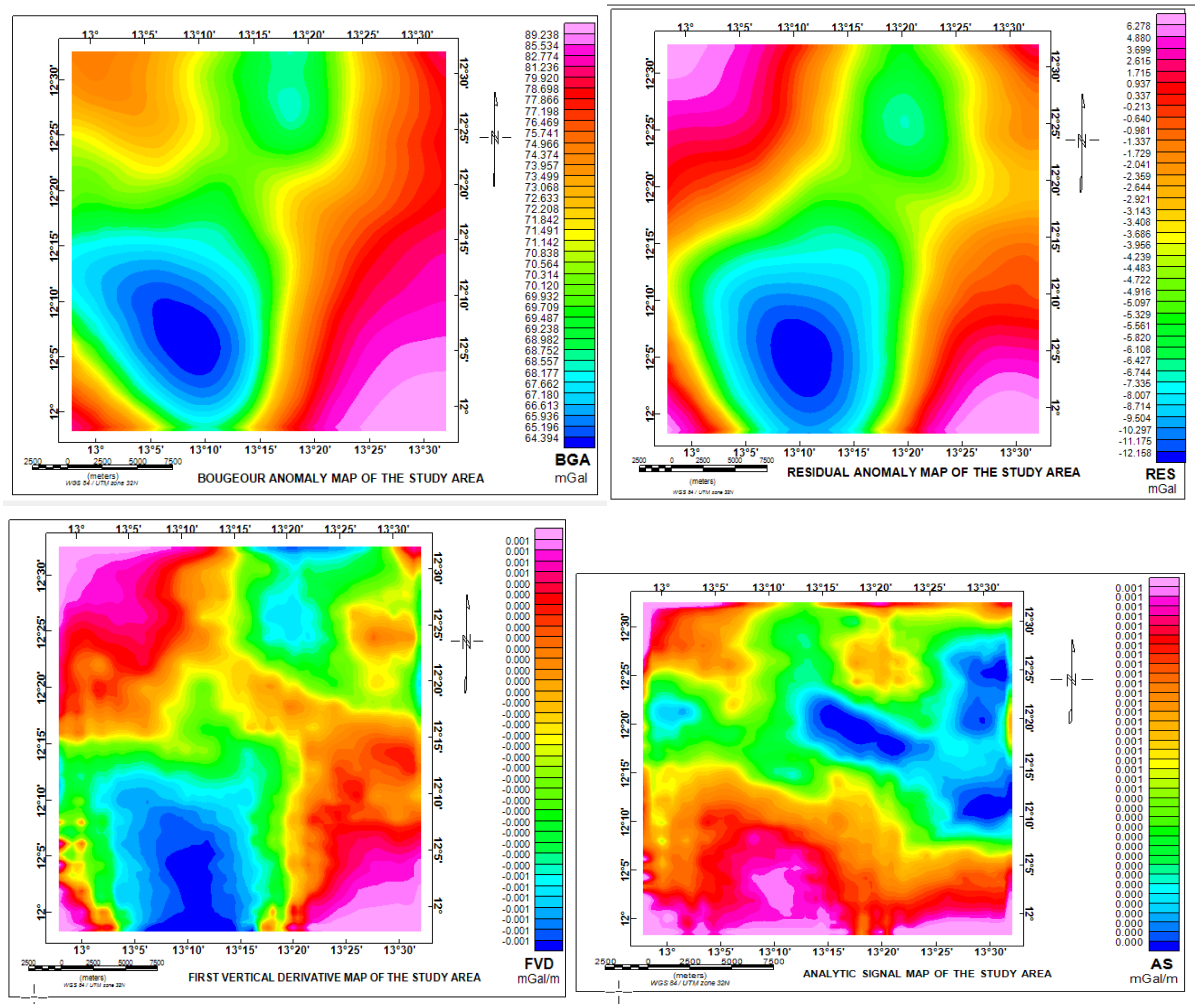

Figure 6: (a) Bouguer Anomaly (b) Residual of Bouguer Anomaly (c) First Vertical derivative and (d) mapAnalytical signal map of the Study Area

VI. REMOTE SENSING METHODS

A. *Lineaments*

The remote sensing lineament Figure 7(a) illustrates a dominant NE–SW and NW–SE structural trendacross the study area, particularly intensearound Nganzai, Ganga Tilo, Mafa**,** Bufejuma, Konduga, and Asula Fura (spanning approximately 12°00′–12°30′N and 13°00′–13°30′E**)**. These anisotropic features represent zones of enhanced crustal fractures, which are critical in geothermal systems as they facilitate deep-seated heat and fluid circulation. Their spatial alignment with hydrothermal alteration zones further underscores their geotectonic significance in geothermal energy prospectivity**.**

B. *Lineament Density*

The lineament density Figure (7b) reveals structurally controlled zones that could act as conduits for geothermal fluid migration. High to very high lineament densities are prominently concentrated along **a** NE–SW and NW–SE structural trend, especially around Nganzai, Ganga Tilo, Mafa, Musari, Abba Jabari, Bufejuma, Konduga, and Asula Fur**a** (coordinates roughly between 12°00′–12°30′N and 13°00′–13°30′E). These structurally deformed regions may signify zones of enhanced permeability and deep-seated heat transfer, thereby marking them as favorable geothermal exploration targets**.**

C. *Hydrothermal Alteration*

The hydrothermal alteration Figure (7c)based on band ratio 6/7 highlights zones of elevated geothermal potential across the northeastern Chad Basin. Areas with very high alteration intensity, notably around Mafa, Masu, Kesangala, Labu, and Asula Fura (between 12°00′N–12°30′N and 13°10′E–13°30′E), indicate significant geothermal activity likely associated with structurally controlled fluid flow and subsurface heat anomalies. The dominant NE–SW and NW–SE trends suggest that fault systems play a key role in directing geothermal circulation. These thermally altered zones represent promising targets for further geothermal exploration and development.

D. *Top of Atmospheric Reflectance*

The Figure (8a)illustrates the top-of-atmosphere reflectance levels across the region. Very low reflectance (dark blue) dominates the southwestern areas like Konduga, Jere, and Fariram (12°00′–12°10′N, 13°00′–13°10′E), while low to moderate reflectance (light blue to beige) covers central zones including Mafa and Kesangala (12°10′–12°20′N, 13°10′–13°20′E). Northern and northeastern parts such as Monguno, Hamrari, and Mangal (12°20′–12°30′N, 13°20′–13°30′E) display high to very high values (orange to red), suggesting greater surface reflectivity in these coordinates.

E. *Brightness Temperature*

The brightness temperature Figure (8b) of the study area, spanning latitudes 12°00′N to 12°30′N and longitudes 13°00′E to 13°30′E, reveals a spatial trend from lower to higher thermal intensity moving from the southwest to the northeast. Areas in the southwest, such as Jere and Konduga, exhibit very low to low brightness temperatures, likely due to vegetation cover or moisture presence.
In contrast, the northeastern and central regions, particularly around Mafa and Monguno LGAs, display moderate to very high values, indicating potential geothermal anomalies or exposed surfaces. The observed thermal gradient suggests zones of possible subsurface heat flow, meriting further geophysical analysis.

F. *Normalised Difference Vegetation Index*

The NDVI Figure (8c)shows vegetation density increasing from the central to the southwestern and northwestern parts of the study area. Very low NDVI values dominate central regions like Mafa, Kesangala, and Asula Fura (12°00′–12°20′ N, 13°10′–13°30′ E), indicating sparse or degraded vegetation, possibly linked to higher land surface temperatures. Higher NDVI values appear in Konduga, Jere, and parts of Nganzai and Monguno (12°00′–12°30′ N, 13°00′–13°10′ E), suggesting healthier vegetation cover. This gradient mirrors the thermal trend, where cooler areas support denser vegetation, reinforcing the land surface–vegetation interaction.

G. *Proportion of Vegetation (PV)*

The Figure (8d)displays the proportion of vegetation across the region using color-coded density levels. Very low vegetation cover (blue) is prominent in the southeastern areas like Mafa, Asula Fura, and Kilborani (12°00′–12°10′N, 13°20′–13°30′E), while low to moderate levels (green to yellow) dominate the central zones around Kesangala and Monguno (12°10′–12°20′N, 13°10′–13°20′E).

©IJRASET: All Rights are Reserved | SJ Impact Factor 7.538 | ISRA Journal Impact Factor 7.894 |

The northwestern parts such as Kuda, Umarniam, and Nganzai (12°20′–12°30′N, 13°00′–13°10′E) show high to very high vegetation proportion (red to pink), indicating denser plant cover in those coordinates.

H. Land Surface Emissivity

The Land Surface Emissivity (LSE) Figure (8e)for northeastern Chad Basin, Nigeria, exhibits significant spatial variability indicative of surface thermal properties relevant to geothermal energy exploration. The emissivity trend suggests that very low to low LSE values (pink to yellow zones) are concentrated in the southern and southeastern portions of the study area, particularly around Doili, Asula Fula, Limna, Mafa, Ajiri, and Kilborani (12°00′N–12°20′N, 13°10′E–13°30′E). These zones are thermally anomalous, where lower emissivity often corresponds to exposed rocky surfaces or dry, thermally active areas, which are potential indicators of elevated subsurface heat flow or geothermal manifestations. Conversely, moderate to high LSE values (green and yellow zones) are dominant in the northwestern and central zones, including towns such as Nganzai, Gajiram, Musari, and Monguno (12°10′N–12°30′N, 13°00′E–13°20′E). These higher emissivity values are associated with denser vegetation and soil moisture, suggesting relatively cooler or thermally stable regions**.**

I. Land Surface Temperature (LST)

The Land Surface Temperature (LST) Figure (8f)shows spatial variation in thermal intensity across the study area, classified from Very Low (dark green) to Very High (red). The temperature distribution reveals a clear northeast to southwest trend, consistent with regional geothermal and tectonic patterns observed in magnetic analyses.

Very High LST zones (red) dominate the southeastern region, particularly around Kilborani, Ajiri, Labe, and parts of Mafa within coordinates 12°00′ to 12°15′ N and 13°20′ to 13°30′ E. These areas may indicate strong geothermal anomalies, potentially associated with near-surface heat sources or active fluid circulation.

High LST (orange) extends across central Mafa to Monguno, especially between 12°10′ to 12°25′ N and 13°10′ to 13°30′ E, highlighting structurally active zones or shallow subsurface heating, possibly linked to magmatic or tectonic processes. Moderate and Low LST zones (yellow to light green) cover the central-west and northern regions, including towns like Zilim, Sugundere, Gajiram, and Kabuluwa, roughly from 12°15′ to 12°30′ N, and 13°00′ to 13°15′ E, suggesting relatively less intense geothermal activity. Very Low LST areas (dark green) appear in the southwestern and western parts of the map (e.g., Konduga, Jere, and Farfaram) within 12°00′ to 12°15′ N and 13°00′ to 13°10′ E, likely representing cooler zones with deeper heat sources or thicker sediment cover.

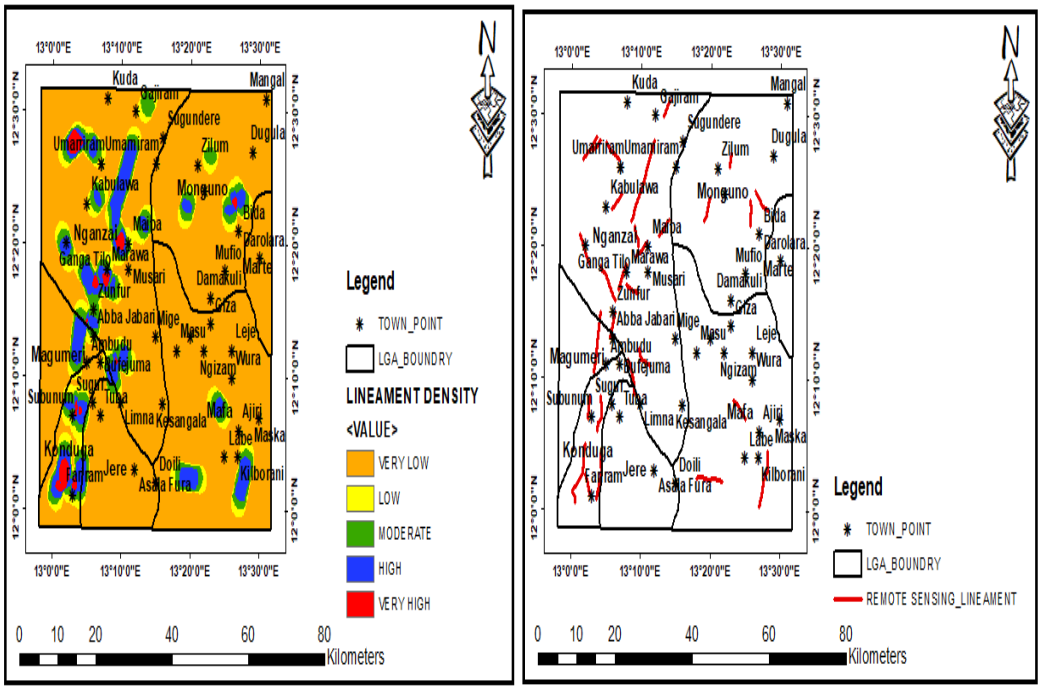

International Journal for Research in Applied Science & Engineering Technology (IJRASET)
ISSN: 2321-9653; IC Value: 45.98; SJ Impact Factor: 7.538
Volume 13 Issue VII July 2025- Available at www.ijraset.com

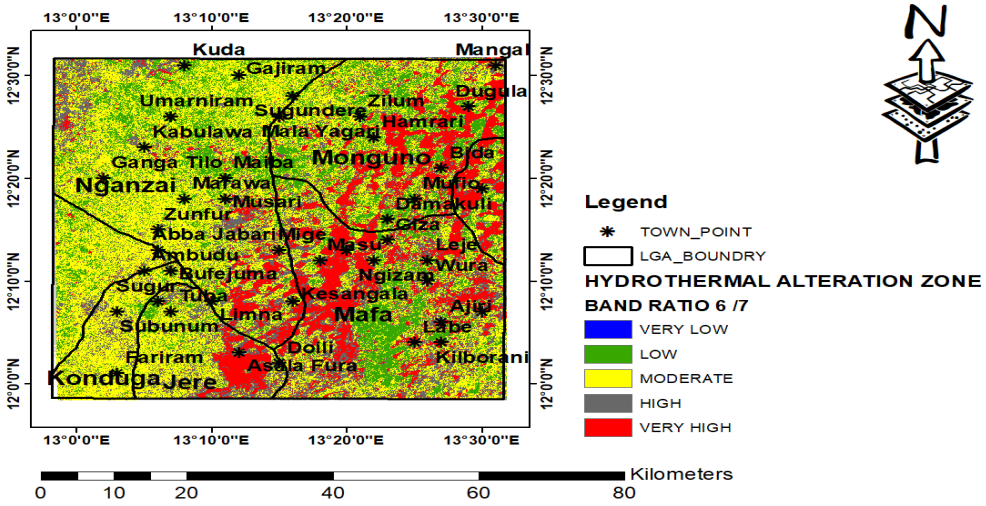

Figure 7: (a) LD lineament Density (b) Lineament (L) and(c) HydrothermalMapof the study area

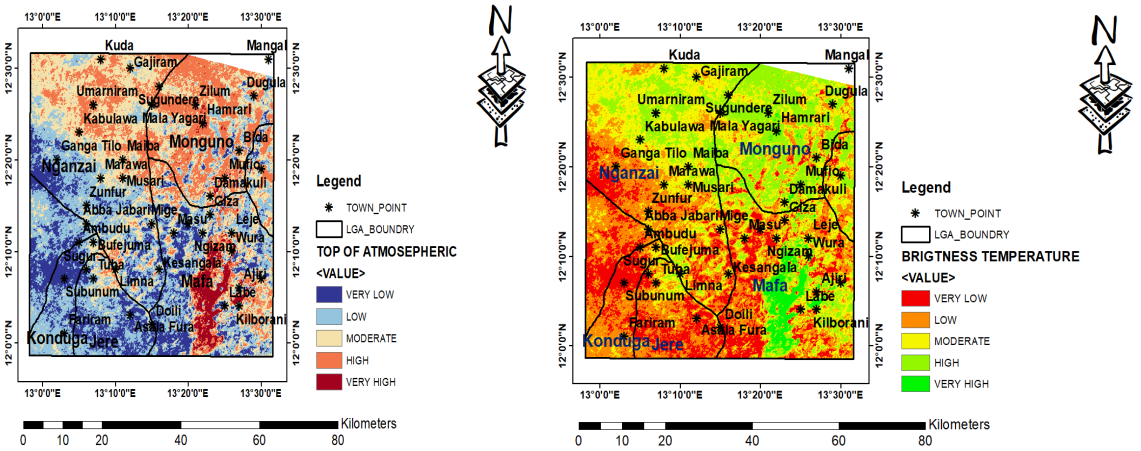

Figure 8: (a) Top of Atmospheric (b) Brightness Temperature Map of the study area

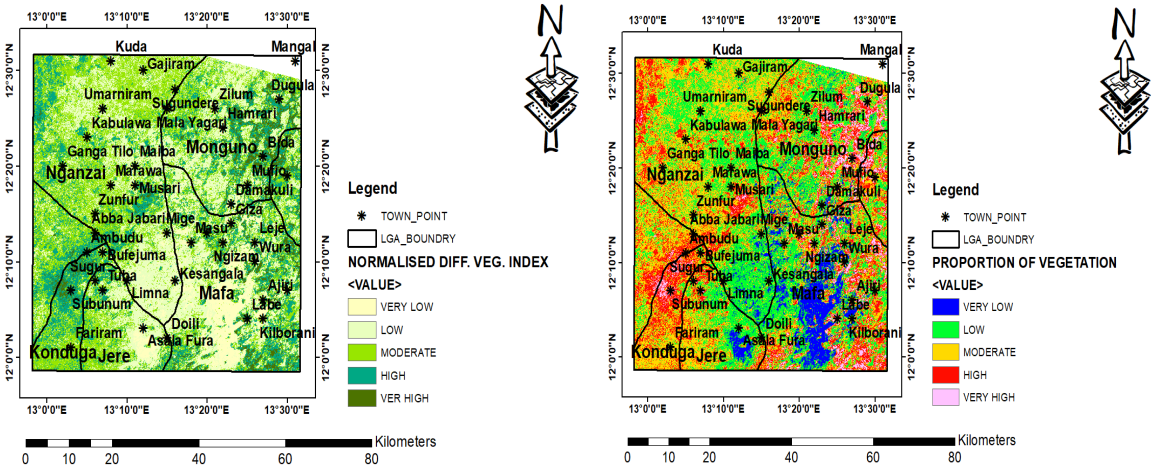

©IJRASET: All Rights are Reserved

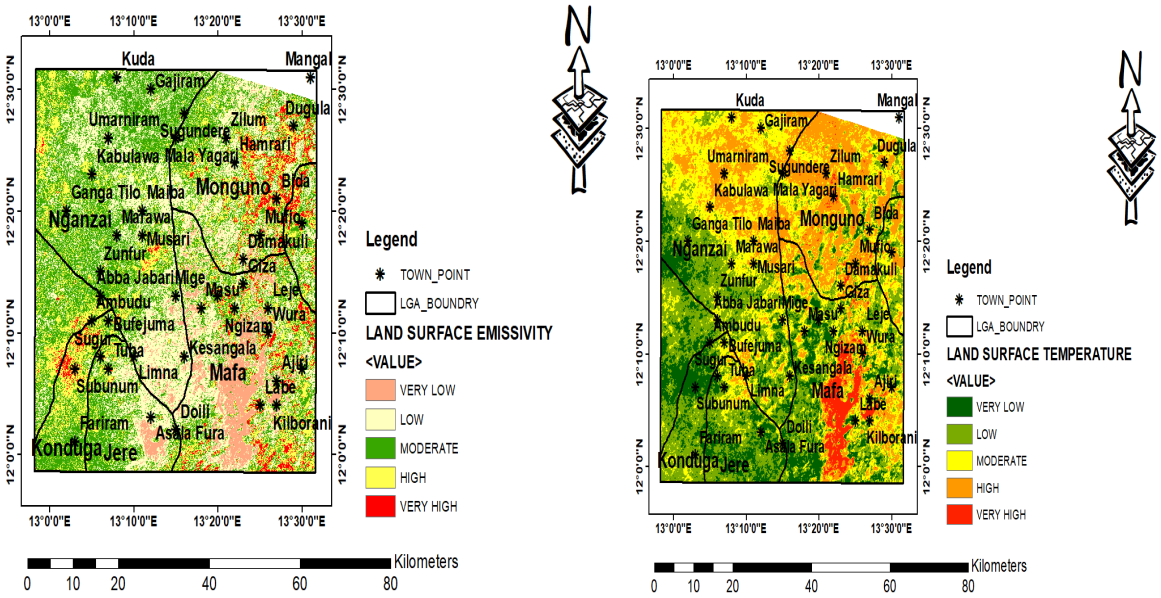

Figure 8: (c) NDVI, (d) Proportion of Veg (e) Land Surface Emissivity and (f) Land Surface Temperature Map of the study area

J. Comparison between Integrated Present Methods and Findings from Previous Studies

1) Magnetic Method: Aeromagnetic data revealed shallow magnetic sources, structural discontinuities, and subsurface intrusions across the central and southwestern sectors. High values in analytic signal and first vertical derivative maps coincide with regions of low Curie depths (as low as 8.49 km) and high geothermal gradients, indicating active heat sources at depth. Notably, Block 2 (centered around 13°22′E, 12°10′N) and Block 6 (around 13°28′E, 12°25′N) show the strongest geothermal indicators, with heat flows over 340 mW/m².

2) Gravity Method: Gravity data reinforce magnetic interpretations, identifying low-density anomalies in the southwestern zones (12°05′N–12°20′N, 13°10′E–13°30′E) that are consistent with thermally altered or fractured rocks. Bouguer anomaly values range between -47.2 and -37.1 mGal. These anomalies align with structural breaks indicated by magnetic trends and remote sensing lineaments, supporting the likelihood of geothermal fluid accumulation and circulation. Gravity-derived vertical derivatives and analytic signals highlight NE–SW and NW–SE fault patterns consistent with geothermal conduits.

3) Remote Sensing Method: Remote sensing analysis confirms the surface expression of geophysical anomalies. High lineament density, significant hydrothermal alterations, and elevated land surface temperatures correspond with underlying magnetic and gravity anomalies. The spatial concurrence of thermal hotspots in LST (ranging from 289.85 to 339.7 K) and brightness temperature maps with low Curie depth and high heat flow zones further validates the subsurface geothermal framework.

Notably, regions such as Mafa (13°22′E, 12°08′N), Kesangala (13°25′E, 12°15′N), and Monguno (13°37′E, 12°40′N) exhibit pronounced surface thermal signatures. Low NDVI and high emissivity in these zones suggest minimal vegetation cover and dry, rocky surfaces typical of thermally active areas.

The present study's spectral analysis across sixteen blocks within the Chad Basin reveals Curie Point Depths (CPD) ranging between 3.94 and 8.48 km, with an average of 6.28 km. These relatively shallow depths suggest a thermally active crust and high geothermal potential. The estimated geothermal gradients span from 68.4 to 147.4 °C/km, averaging 96.4 °C/km, while heat flow values range between 170.93 and 368.39 mW/m², with a mean of 241.04 mW/m². Notably, Blocks 2 and 6 (centered around, 13.2°E, 12.2°N) exhibit the shallowest CPDs and highest heat flow, indicating localized geothermal anomalies associated with structural weaknesses and magmatic activity.

These results reflect significantly more intense geothermal activity compared to previous studies in the Chad Basin. For instance, Lawal et al. (2018) estimated CPD values between 15.14 and 33.46 km, geothermal gradients ranging from 17.02 to 38.34 °C/km, and heat flow values between 39.37 and 95.85 mW/m². Similarly, Anakwuba et al. (2016) reported CPDs between 10.63 and 20.07 km in Gubio (Northwest Chad Basin), with geothermal gradients of 28.9–54.6 °C/km (average ~40.3 °C/km) and heat flows of 72.2–136.4 mW/m² (average ~100.7 mW/m²).

Earlier studies by Onuoha and Ofoegbu (1985) and Ajakaiye et al. (1991) also noted crustal thinning and elevated heat flow, but their estimates were constrained by lower-resolution data, typically reporting CPDs between 16 and 25 km, and heat flow values ranging from 60 to 110 mW/m². Recent spectral studies using gravity data (e.g., Yaya et al., 2021**)** found CPDs of 5.77–13 km (mean 9.21 km), geothermal gradients between 44.6 and 107.2 °C/km (mean ~75.9 °C/km), and heat flow values between 111.6 and 268 mW/m² (mean ~189.8 mW/m²).

Additional insights from thermal gradient logging and heat flow analysis, such as those by Avbovbo (1978) and Onuoha and Kingston (1989)**,** indicated regional geothermal gradients between 2.8 and 5.9 °C/100 m and corresponding heat flows ranging from 45 to 90 mW/m² across the Nigerian sector of the basin. More recent multi-disciplinary remote sensing studies, including Musa et al. (2023) and Idris Nda et al. (2022)**,** emphasized the use of Land Surface Temperature (LST), NDVI, and emissivity data but lacked integration with high-resolution geophysical models.

In general, the present study surpasses earlier investigations both in spatial resolution and interpretative integration. The synergy of aeromagnetic, gravity, and remote sensing datasets provides robust evidence of shallow-sourced heat anomalies and defines structurally controlled geothermal provinces, especially in the central and southwestern Chad Basin. These findings validate the effectiveness of integrated geospatial approaches in delineating geothermal potential in intracratonic basins.

VII. CONCLUSION

The integration of aeromagnetic, gravity, and remote sensing techniques has revealed a coherent geothermal framework within the northeastern Chad Basin. Magnetic data indicate shallow intrusions, fault zones, and high Curie point temperatures, particularly in the southwestern and central areas (12°00′N–12°30′N, 13°00′E–13°30′E), where elevated geothermal gradients and heat flows suggest viable geothermal reservoirs. Gravity anomalies confirm the presence of fractured, low density rocks and delineate major structural corridors aligned with mapped lineaments. Remote sensing data reinforce these findings by identifying areas of intense hydrothermal alteration, low vegetation indices, and high surface temperatures, especially in Mafa (13°22′E, 12°08′N), Kesangala (13°25′E, 12°15′N), and Kilborani (13°28′E, 12°20′N). The convergence of high heat flow, shallow Curie depths, significant structural deformation, and thermal anomalies strongly supports the presence of economically exploitable geothermal resources. This multidisciplinary approach provides a robust framework for future geothermal exploration in the region.

REFERENCES

[1] Ajakaiye, D. E., Ojo, S. B., & Okereke, C. S. (1991). Crustal structure of the Benue Trough, Nigeria in relation to geothermal prospects. Tectonophysics, 34, 61–79.
[2] Anakwuba, E. K., Chinwuko, A. I., Onuba, L. N., & Okolie, E. C. (2016). Estimation of heat flow and geothermal gradient from spectral analysis of aeromagnetic data over Gubio area, Chad Basin Nigeria. SN Applied Sciences,
[3] Avbovbo, A. A. (1978). Geothermal gradients in the southern Nigerian Basin. Bulletin of Canadian Petroleum Geology, 26, 268–274.
[4] Baioumy, H., & Tada, S. (2022). Geothermal energy exploration using remote sensing and geophysical data: A case study from the Eastern Desert, Egypt. Renewable Energy, 181, 1279–1293. https://doi.org/10.1016/j.renene.2021.09.085
[5] Blakely, R. J. (1996). Potential theory in gravity and magnetic applications. Cambridge University Press.
[6] Chander, G., Markham, B. L., & Helder, D. L. (2009). Summary of current radiometric calibration coefficients for Landsat sensors. Remote Sensing of Environment, 113(5), 893–903.
[7] DiPippo, R. (2015). Geothermal Power Plants: Principles, Applications, Case Studies and Environmental Impact. Butterworth-Heinemann.
[8] DiPippo, R. (2016). Geothermal power generation: Developments and innovation. Woodhead Publishing.
[9] Ebong, I. D., Ugwu, G. Z., & Igboekwe, M. U. (2022). Aeromagnetic modeling of heat flow potential in parts of the Lower Benue Trough, Nigeria. Geothermics, 103, 102428.
[10] Eppelbaum, L. V., Kutasov, I., & Pilchin, A. (2014). Applied Geothermics. Springer.
[11] Fedi, M., & Florio, G. (2001). Detection of potential field's source boundaries by enhanced horizontal derivative method. Geophysical Prospecting, 49(1), 40–58.
[12] Guha, A., Weng, Q., & Lo, C. P. (2013). Analysis of land surface temperature–vegetation patterns using MODIS satellite data. Environmental Earth Sciences, 68(8), 2399–2410.
[13] Hinze, W. J., von Frese, R. R. B., & Saad, A. H. (2013). Gravity and Magnetic Exploration: Principles, Practices, and Applications. Cambridge University Press.
[14] IEA. (2022). Geothermal power and heat. International Energy Agency. https://www.iea.org/reports/geothermal-power
[15] Idris Nda, A., Musa, M., & Abdullahi, A. (2022). Application of remote sensing techniques for geothermal resource exploration in the Nigerian Chad Basin. Journal of Geosciences and Geomatics, 10(2), 87–94.
[16] Jiménez-Muñoz, J. C., Sobrino, J. A., & Gillespie, A. (2009). Enhanced split-window algorithm for land surface temperature retrieval from remote sensing data. Remote Sensing of Environment, 112(6), 2367–2383.
[17] Lawal, K. M., Onuba, L. N., Anakwuba, E. K., & Chinwuko, A. I. (2018). Geothermal energy potential evaluation from aeromagnetic data of parts of Chad Basin Nigeria. International Journal of Geophysics, 2018, 1–12.

[18] Lund, J. W., & Boyd, T. L. (2016). Direct utilization of geothermal energy 2015 worldwide review. Geothermics, 60, 66–93.
[19] Lund, J. W., & Toth, A. N. (2021). Direct utilization of geothermal energy 2020 worldwide review. Geothermics, 90, 102020.
[20] Mallick, J., Kant, Y., & Bharath, B. D. (2008). Estimation of land surface temperature over Delhi using Landsat-7 ETM+. Journal of the Indian Geophysical Union, 12(3), 131–140.
[21] Mogaji, K. A., Lim, H. S., Abdullar, K. B., & Aladesanmi, A. O. (2017). Integrated approach to geothermal exploration using geophysical and remote sensing techniques: Case study of North Central Nigeria. Journal of African Earth Sciences, 127, 27–44.
[22] Musa, M., Usman, A. A., & Idris, A. N. (2023). Remote sensing-based identification of potential geothermal zones in Borno State, Nigeria. African Journal of Environmental Science and Technology, 17(5), 145–156.
[23] Noorollahi, Y., Fadai, D., & Rosen, M. A. (2008). Geothermal energy development in Iran: A review of current status and future plans. Renewable and Sustainable Energy Reviews, 12(4), 1001–1009.
[24] Noorollahi, Y., Itoi, R., Fujii, H., & Tanaka, T. (2008). GIS model for geothermal resource exploration in Akita and Iwate prefectures, northern Japan. Computers & Geosciences, 34(10), 1587–1597.
[25] Nwankwo, C. N., Akpan, A. E., & Onwuemesi, A. G. (2012). Geothermal gradients and subsurface temperatures in the Anambra Basin, southeastern Nigeria. Journal of African Earth Sciences, 65, 73–78.
[26] Nwankwo, C. N., Ugwu, G. Z., & Onuba, L. N. (2012). Estimation of geothermal gradients and heat flow in the Sokoto Basin of Northwestern Nigeria. Journal of Applied Geophysics, 88, 1–8.
[27] Onuoha, K. M., & Kingston, G. S. (1989). Heat flow and geothermal gradient in the Anambra Basin of Nigeria. Geothermics, 18(2), 165–175.
[28] Onuoha, K. M., & Ofoegbu, C. O. (1985). Crustal thickness in the Chad Basin, Nigeria, from gravity interpretation. Geophysics, 50(2), 326–333.
[29] Pettorelli, N., et al. (2005). Using NDVI to assess ecological responses to environmental change. Trends in Ecology & Evolution, 20(9), 503–510.
[30] Quintero, R., Muñoz, G., & Martínez, R. (2019). Integration of gravity, magnetic and remote sensing data for geothermal exploration in the Andes. Geothermics, 80, 123–134.
[31] Reeves, C. V. (2005). Aeromagnetic Surveys: Principles, Practice and Interpretation. Geosoft Inc.
[32] Sadeghi, H., Noorollahi, Y., & Ghasemi, H. (2023). Integration of remote sensing and geophysical data in geothermal exploration: A case study. Renewable Energy, 205, 1007–1021.
[33] Sandwell, D. T., Müller, R. D., Smith, W. H. F., Garcia, E., & Francis, R. (2013). New global marine gravity model from CryoSat-2 and Jason-1 reveals buried tectonic structure. Science, 346(6205), 65–67.
[34] Sobrino, J. A., Jiménez-Muñoz, J. C., & Paolini, L. (2004). Land surface temperature retrieval from LANDSAT TM 5. Remote Sensing of Environment, 90(4), 434–440.
[35] Sobrino, J. A., Jiménez-Muñoz, J. C., & Paolini, L. (2004). Land surface temperature retrieval from Landsat TM 5. Remote Sensing of Environment, 90(4), 434–440.
[36] State, N. M. (2021). Nigeria's Renewable Energy Master Plan: Review and recommendations. Nigerian Energy Commission. https://www.energy.gov.ng
[37] Telford, W. M., Geldart, L. P., & Sheriff, R. E. (1990). Applied Geophysics (2nd ed.). Cambridge University Press.
[38] Tucker, C. J. (1979). Red and photographic infrared linear combinations for monitoring vegetation. Remote Sensing of Environment, 8(2), 127–150.
[39] Weng, Q. (2009). Thermal infrared remote sensing for urban climate and environmental studies: Methods and applications. ISPRS Journal of Photogrammetry and Remote Sensing, 64(4), 335–344.
[40] Yaya, A., Alabi, A. A., & Alao, S. A. (2021). Curie point depth and geothermal assessment using gravity data: A case study of the northern Nigerian Chad Basin. International Journal of Science and Research (IJSR), 10(5), 1330–1339.

©IJRASET: All Rights are Reserved | SJ Impact Factor 7.538 | ISRA Journal Impact Factor 7.894 |

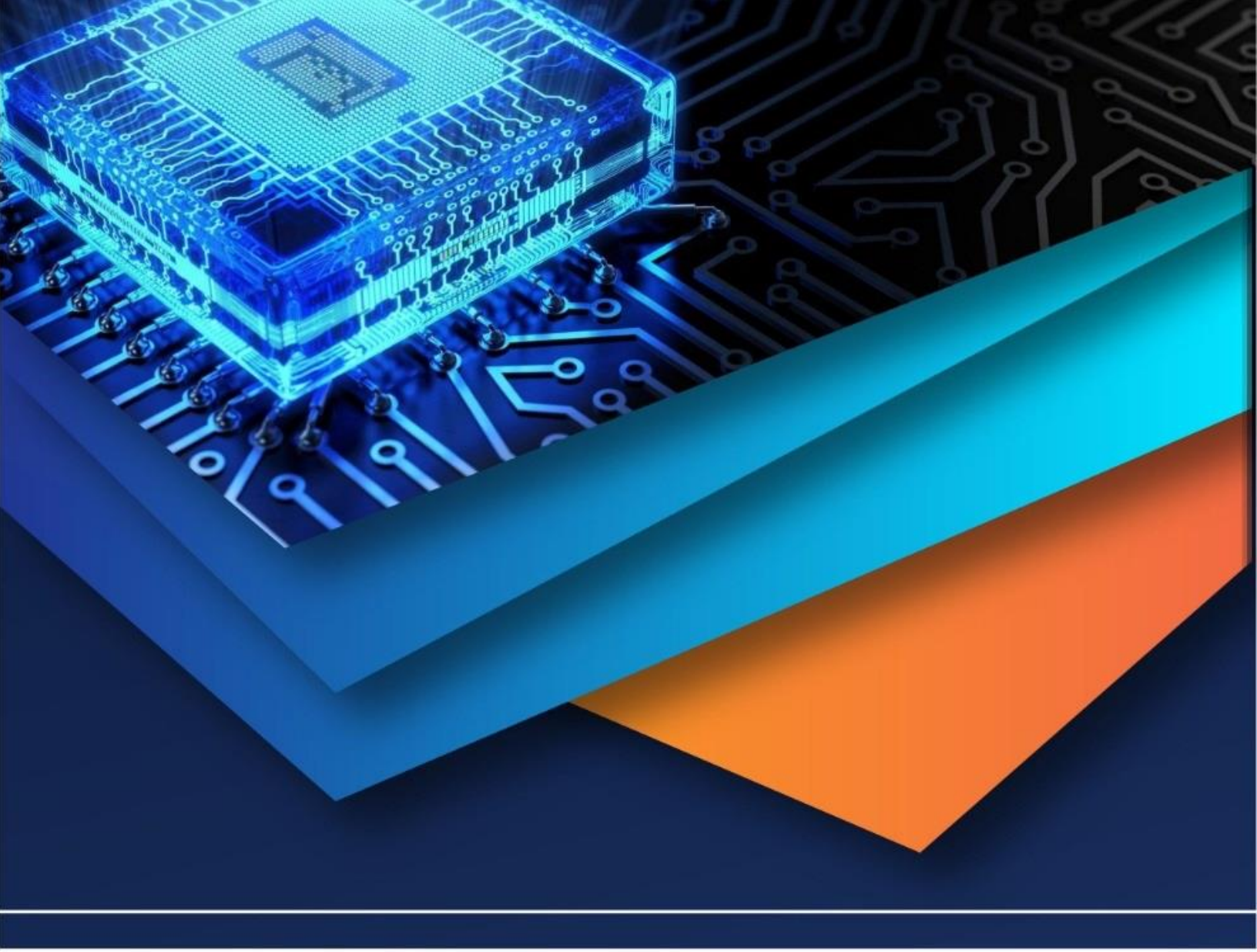

10.22214/IJRASET

45.98

IMPACT FACTOR: 7.129

IMPACT FACTOR: 7.429

INTERNATIONAL JOURNAL FOR RESEARCH

IN APPLIED SCIENCE & ENGINEERING TECHNOLOGY

Call : 08813907089 (24*7 Support on Whatsapp)